Characterization of terahertz wavefront aberrations using computational shear-interferometry

Mostafa Agour[a,b,*], **Claas Falldorf**[a], **Fatima Taleb**[c], **Enrique Castro-Camus**[c], **Martin Koch**[c], **Ralf B. Bergmann**[a,d]

[a]BIAS-Bremer Institut für angewandte Strahltechnik, 28359 Bremen, Germany
[b]Aswan University, Faculty of Science, Department of physics, 81528 Aswan, Egypt
[c]Faculty of Physics and Material Sciences Center, Philipps-Universität Marburg, Renthof 5, 35032 Marburg, Germany
[d]University of Bremen, MAPEX Center for Materials and Processes and Faculty of Physics and Electrical Engineering, 28359 Bremen, Germany

Abstract. We propose a new solution for sensing a terahertz (THz) wavefront based on a THz reference-less shear interferometer. The key component of the experimental configuration of the proposed interferometer is a THz Ronchi phase grating (RPG). The RPG is custom designed and fabricated for a 0.28 THz source using mechanical milling on a block of high-density polyethylene (HDPE) with a computer numerical control (CNC) machine. It acts as a shearing element that generates two diffraction orders, thereby creating two laterally shifted copies of the investigated wavefront in the sensor plane where a THz camera is placed. The direction of the shear can be varied by rotating the grating. Since the grating is a phase grating, the diffraction efficiency is very high. The approach is verified experimentally by demonstrating interferograms of a spherical wave and wavefront reconstruction from five different shears using a gradient-based iterative process.

Keywords: Terahertz wavefront, shear-interferometry, phase grating, wavefront sensing, phase measurements, wavefront aberrations.

*Mostafa Agour, agour@bias.de

1 Introduction

Terahertz (THz) radiation has attracted the attention of a broad set of researchers because it has interesting properties compared to other spectral bands.[1,2] For instance, unlike x-rays, THz-waves are non-ionizing and thus harmless for biological tissues. For this reason non-destructive testing for the identification of substances[3,4] as well as imaging applications[5–7] have been the subject of intense research recently. THz-waves penetrate a wide range of material packages which are optically opaque in the visible or near infrared bands. These properties open interesting possibilities for non-destructive testing in order to inspect agricultural products and food,[8–11] medical imaging,[12–14] and communication.[15–20] In turn, the appearance of all these applications has driven the development of new techniques, THz quasi-optical components, as well as sources and detectors.

Sensing both, the amplitude and also the phase of THz radiation, plays an important role to improve the applicability of THz in many areas, such as quality control[21] and biology.[22] This has been achieved by the use of THz time-domain spectroscopy as well THz digital holography (DH). There are many detection methods for THz beams, among them, full-field single beam methods such as in-line holography, iterative and deterministic multiple plane phase retrieval (PR)[23–25] and ptychography[26] have been used. However, these techniques require holograms or intensity patterns of the diffracted wave field to be recorded across different planes, in analogy to the implementation in the visible band in order to solve the associated inverse reconstruction problem.[27–30] As

an example, in-line THz DH suffers from the overlapping of the zero-order and twin-image artifacts reducing the resolution of the reconstruction, which one can overcome by capturing multiple in-line holograms across different axial planes. Thus, in in-line DH, PR and ptychography the recording process is time consuming and is highly sensitive to mechanical vibration. Moreover, the reconstruction process for, both PR and ptychography, is based on the presence of diversity of the captured intensity patterns. Consequentially, smooth wavefronts, such as plane waves, can not be analyzed. Furthermore, off-axis THz-DH, requires a reference wave with known characteristics and both temporally and spatially coherent illumination since it is based on the interference of diffracted light with a reference wave. This constitutes considerable drawbacks, because the characterization of an *a-priori* unknown THz wavefront emitted by an antenna or self-luminous object, is challenging and in some cases is not possible.

In this paper, we propose a method to circumvent these requirements based on a THz referenceless shear interferometer realized by a THz Ronchi phase grating (RPG) between the THz source and the camera sensor. In analogy to grating-based shear interferometers realized in visible range,[31,32] the RPG[33] acts as a shearing element that generates two diffraction orders, thereby creating two laterally shifted images in the sensor plane. The direction of the shear can be varied by rotating the grating. Since the RPG is a phase grating, the diffraction efficiency is very high and approximately 80% of the diffracted light falls on the ± 1 diffraction orders.

In contrast to our earlier work we do not employ a $4f$-setup as was used in an earlier publication[34] or other imaging elements. Since no imaging system is used, the setup is aberration free and therefore only measures the properties of the wavefield approaching the RPG. For this purpose, five different shear measurements are acquired. With these measurements, the wavefront reconstruction is achieved using a gradient-based iterative process. Also in contrast to another of our earlier publications[35] here, we broaden the content by generalizing the proposed method to enable the measuring of wavefront aberrations not influenced by aberrations of the system itself. In addition, we provide a quantitative assessment of the proposed method.

2 THz shear interferometer setup

Figure 1 shows a schematic of a simple common-path shear interferometer. It consists of three main components i) a continuous wave (CW) THz-source and a lens that introduces spherical aberrations, ii) a Ronchi phase grating (RPG) which introduces the shear and iii) a THz camera line-sensor.

The distance between the source and the lens is given by z_1, while z_2 is the distance between the lens and the RGP, and z_3 is the distance between the RPG and the camera. Such a simple setup is used here for measuring THz spherical wavefronts as well as spherical aberrations. Lets assume that the emitter is a point source which generates a spherical wave with U_1 being the spherical wave field directly at the front of the RPG. Thereafter, U_1 is modulated by the transmittance G of the RPG and a modified wave field U_2 is generated directly behind the RPG. Such a modified wave field then propagates to generate a new wave field $U = \mathcal{P}\{U_2\}$ at the camera plane, where $\mathcal{P}$ is a propagation operator used to propagate the modulated wave field to the camera plane.

Figure 2 shows a scheme of the grating for illustration purposes. Since the RPG is the key component of the setup, we discuss its properties here in more detail. Lets assume an RPG with a

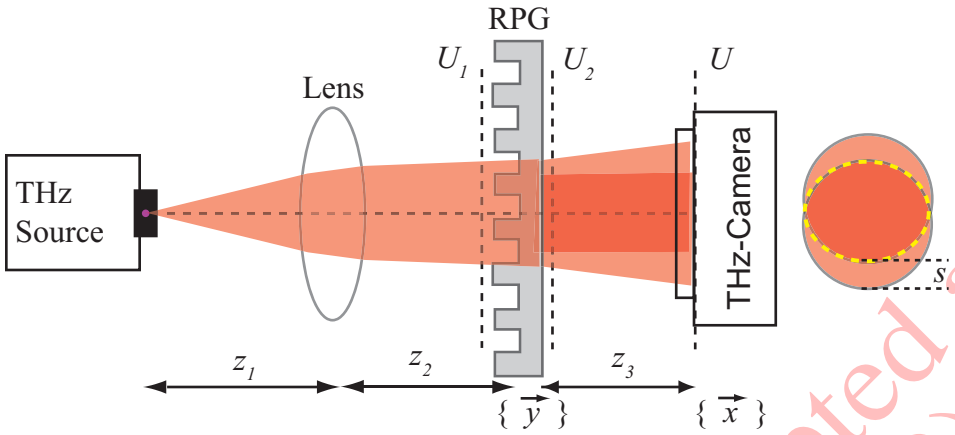

Fig 1 Schematic of the experimental configuration used to measure the THz wavefronts. U_1 and U_2 are the complex amplitude of the wave field before and after transmitted through the a Ronchi phase grating (RPG) inserted in the plane $\{\vec{y}\}$ which is z_1 away from the THz source. The wave field U is generated across the output plane $\{\vec{x}\}$ where a THz camera sensor is used to capture the interference pattern generated from the overlap between the ± 1 diffraction orders of the RPG. At a distance of z_3 from the RPG the two ± 1 diffraction orders are separated by s which refers to as the shear.

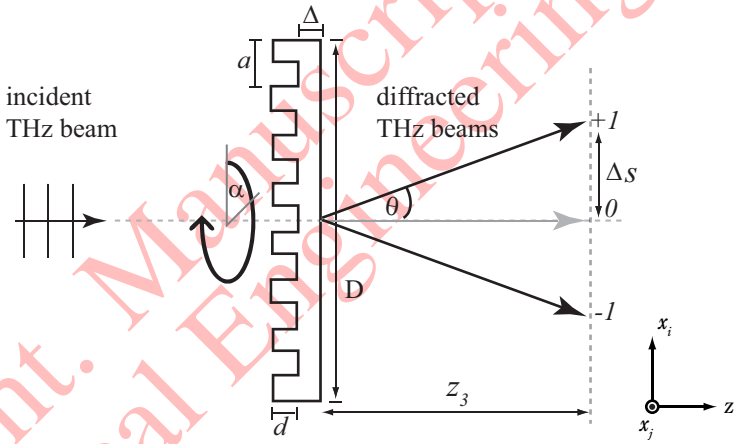

Fig 2 Schematic representation of the THz beam diffraction by a phase Ronchi grating. The Ronchi grating has a clear aperture of a diameter (D), and a thickness of (Δ), a grating period of a, a depth (height of the groves) of d. The $+1$, 0 and -1 refer to the diffraction orders of the grating, θ represents the diffraction angle, Δs represents the half of the shear s and α is the rotation angle used to change the direction of the shear. For ideal depth d for a given wavelength the Phase Ronchi grating diffracts no substantial intensity into the 0 order.

clear aperture of D and grating period of a. The grating vector $\vec{g}$ defined as

$$\vec{g} = \frac{1}{a}\begin{pmatrix}\sin\alpha\\ \cos\alpha\end{pmatrix}, \tag{1}$$

depends on the grating orientation α and the period a, the grating modulations for the $+1$ and -1 diffraction orders is given as $G_{+1} = \exp(\mathrm{i}2\pi\vec{g}\vec{x})$ and $G_{-1} = \exp(-\mathrm{i}2\pi\vec{g}\vec{x})$. Accordingly, the

wave field U_c generated from the coherent superposition of the $+1$ and -1 diffraction orders can be written as

$$U_c(\vec{x}) = U_{+1}(\vec{x}) + U_{-1}(\vec{x}) = U(\vec{x}) \cdot \exp\left(\mathrm{i}2\pi\vec{g}\vec{x}\right) + U(\vec{x}) \cdot \exp\left(-\mathrm{i}2\pi\vec{g}\vec{x}\right) . \tag{2}$$

Thus, light diffracted to the two orders is modified with different linear phase ramps. Because we aim to fabricate an optimal RPG, the phase modulation introduced to the beam passing through it is important. Such a phase modulation is introduced by the periodically varying depth d of the grating which leads to a phase difference ϕ of

$$\phi = \frac{2\pi}{\lambda}(n-1)d\,, \tag{3}$$

where λ is the wavelength of the THz beam, n is the refractive index of the grating material and d is the depth of the grooves at the grating. Minimizing the diffraction efficiency of the 0-th and the even diffraction orders requires that the phase difference $\phi = \pi$. Substituting this condition in Eq. (3) yields the ideal depth of the grating grooves to

$$d = \frac{\lambda}{2(n-1)} . \tag{4}$$

Such a grating structure will lead to a diffraction angle θ of

$$\theta = \sin^{-1}\left(\frac{\lambda}{a}\right), \tag{5}$$

for the $+1$ and -1 diffraction orders respectively, assuming normal incidence to the grating surface. This angle causes the shift Δs of the $+1$ diffraction order at a distance of z_3 from the optical axis which can be calculated as

$$\Delta s = \frac{\lambda z_3}{a}\,, \tag{6}$$

where the distance z_3 is the distance between the grating and the camera sensor and assuming $z_3 >> s$. Accordingly, we can obtain the shear $s = 2\Delta s$ between the $+1$ and -1 diffraction orders. Thus, the wave field modulation by the RPG produces two mutually shifted copies of the wave field. Across the overlap zone between these two copies, as shown in Fig. 1, an interference pattern across the camera plane is generated. As an application, the characterization of the THz beam across the camera plane by measuring the amplitude and the wavefront will be discussed. For a spherical wave field propagating thought the setup, the spherical wave generated at the camera plane U_s can be written according to the Fresnel approximation as

$$U_s(\vec{x}) = \frac{A(\vec{x})}{z} \cdot \exp\left[\mathrm{i}kz\left(1 + \frac{|\vec{x}|^2}{2z^2}\right)\right] . \tag{7}$$

Where, $A(\vec{x})$ is the real amplitude of the spherical wave, $k = 2\pi/\lambda$ denotes the wavenumber and $z = z_1 + z_2 + z_3$ is the distance between the THz source and the camera which in turn gives the beam radius of curvature. Notice that, since this is a special case, the linear ramp modulation at the camera plane given by Eq. (2) leads to a shift of the test spherical wavefront. Accordingly, the

intensity $I(\vec{x})$ of the interference pattern may be written as

$$\begin{aligned} I(\vec{x}) = |U_c(\vec{x})|^2 &= \left| U_s\left(\vec{x} - \frac{\vec{s}}{2}\right) + U_s\left(\vec{x} + \frac{\vec{s}}{2}\right) \right|^2 \\ &= I_0(\vec{x}) + 2\mathcal{R}\left\{ U_s^*\left(\vec{x} - \frac{\vec{s}}{2}\right) U_s\left(\vec{x} + \frac{\vec{s}}{2}\right) \right\}, \end{aligned} \tag{8}$$

here, $I_0(\vec{x}) = 2|A(\vec{x})|^2/z^2$ is the background intensity assuming equal amplitudes of the two copies of the test wave field, $\mathcal{R}\{\cdots\}$ refers to as the real part of a complex number and $*$ refers to the complex conjugate. $\mathcal{R}\{\cdots\}$ represents the interference terms which contain the phase information. Substituting Eq. (7) into Eq. (8), the interference term takes the form

$$U_s^*\left(\vec{x} - \frac{\vec{s}}{2}\right) U_s\left(\vec{x} + \frac{\vec{s}}{2}\right) = B(\vec{x}) \cdot \exp\left(\mathrm{i}\frac{k}{z}\vec{s}\cdot\vec{x}\right). \tag{9}$$

with the intensity envelop

$$B(\vec{x}) = \frac{1}{z^2} A\left(\vec{x} - \vec{s}/2\right) A\left(\vec{x} + \vec{s}/2\right) \tag{10}$$

and the second part of Eq. (9) being a linear phase ramp which depends both on the beam radius of curvature z and the shear $\vec{s}$. The ramp implies that the linear fringes of the interference pattern have a spatial carrier frequency of

$$\vec{\xi} = \frac{k\vec{s}}{2\pi z} = \frac{\vec{s}}{\lambda z}. \tag{11}$$

Equation (11) can be used in order to determine the shear s directly by taking the Fourier transform of the corresponding interference pattern. Hereafter, the shift Δ_ξ of the peaks across the Fourier domain is determined and thus the shear is

$$\vec{s} = \frac{\vec{\Delta}_\xi \lambda z}{N \Delta x}. \tag{12}$$

Here, N and Δx are the number of camera pixels in one direction and the pixel pitch, respectively.

3 Experimental results and discussions

3.1 Experimental setup and the recorded interferograms

Figure 3 shows the experimental setup based on the scheme shown in Fig. 1. An impact ionization avalanche transit time (IMPATT) diode from TeraSense Corp. is used as a THz source which emits a linearly polarized radiation at 280 GHz, ($\lambda = 1.07$ mm). A high gain diagonal horn serves to generate a Gaussian beam. The power coupled out is about 40 mW measured directly behind the horn. The emitting spherical waves propagate through the RPG fabricated using mechanical milling on a block of high-density polyethylene (HDPE) with a computer numerical control (CNC) machine. The RPG has a period of $a = 6.44$ mm and is optimized for the 280 GHz beam.[33] The distance between the horn and the lens of 200 mm focal length is $z_1 = 45$ mm, $z_2 = 100$ mm. A line-array GaAs plasmonic THz camera TeraSense Corp. consisting of 256 pixels with a pixel pitch of $\Delta x = 0.5$ mm is located at the output plane at $z_3 = 147$ mm from the RPG. Such a construction generates a spherical wavefront at the sensor plane having 305 mm radius of curvature. To acquire

two dimensional (2D) images, the sensor was scanned along the horizontal axis using a translation stage supplied by Physik Instrumente (PI). It is noted that to achieve the optimum interference contrast, the polarization direction of the radiation is selected to match the preferred direction of the GaAs plasmonic terahertz detector.

Three sets of measurements were performed to measure different wavefont aberrations: The first shear measurement was done in order to measure a spherical wavefront. Here the setup is aligned aiming to generate a test spherical wavefront at the sensor plane with a radius of curvature of $305\,\mathrm{mm}$ as mentioned above. For the second shear measurement the THz source was laterally shifted in order to produce a tilted spherical wavefront. The third shear experiment was performed by rotating the $200\,\mathrm{mm}$ plano-convex lens around an axis normal to its optical axis, in order to generate astigmatism aberration to the spherical wavefront.

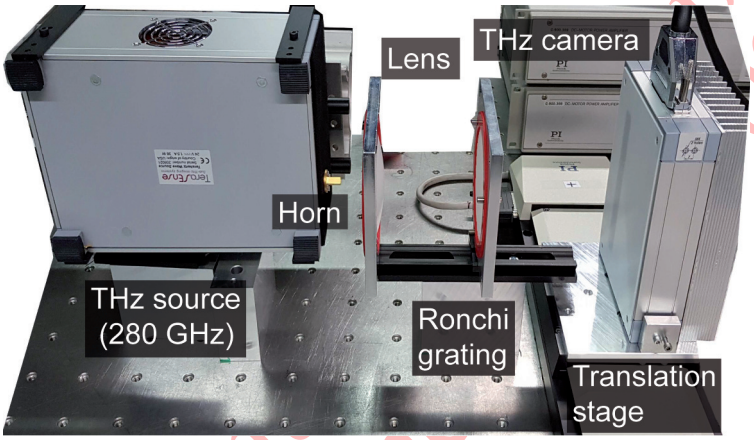

Fig 3 Photograph of the experimental shear interferometer setup. A continuous wave THz source emits a spherical wave at 280 GHz. A detachable high gain diagonal horn shapes the amplitude of the emitted spherical wave to a Gaussian envelope. The RPG, i.e the shear element, is inserted between the source and the line camera creating an overlap between the two copies of the test spherical wave. An intensity image of the wave field is recorded by moving the THz camera using a translation stage.

Figure 4 shows examples of the recorded intensity patterns of the first shear experiment: The intensity profile of the test spherical wave field is shown in (a) and two interferograms resulting from the interference of the two shifted spherical wave fields for two different shears are shown in (b) and (c), respectively. The recorded intensity profile of the investigated spherical wave field has a Gaussian profile. The two shears applied to capture the images shown in (b) and (c) are $s_0 = [-44, 0]\,\mathrm{mm}$ and $s_4 = [-30, 32.5]\,\mathrm{mm}$ obtained by rotating the RPG by $42°$. As shown in Fig. 4, the interference patterns are composed of linear fringes generated in the overlap zone as theoretically expected from the coherent superposition of two shifted spherical wave fields. However, as shown in[33] there is 4.15% of the light diffracted to the 0 order which is approximately equal to the light reflected from a glass surface in standard interferometers. Thus, the superposition of the $+1$, -1, and 0 orders generate the interference patterns. Rising the 0 order modulates the interference patterns by changing the maximum intensity over the fringes as seen in Fig. 4(b,c), this given that the interference fringes resulting from $+1$ and 0 or -1 and 0 have half of the $+1$ and -1 interference frequency.

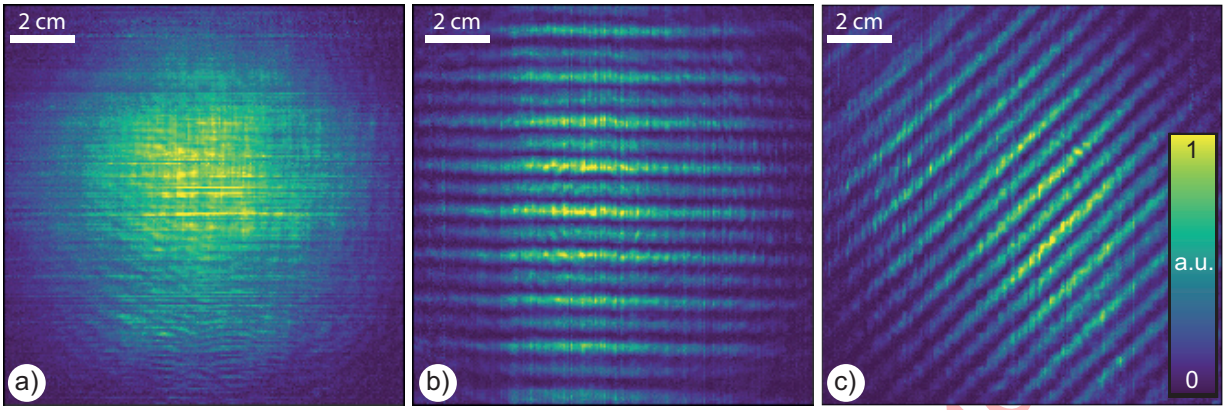

Fig 4 Captured intensity patterns: a) Intensity profile of the spherical wave captured at an equivalent distance of 305 mm from the source in the absence of RPG consistent with a Gaussian intensity envelope. b) and c) Two examples of the intensity interferograms captured after readjusting the RPG between the source and the camera for the shears $s_0 = [-44, 0]$ mm and $s_4 = [-30, 32.5]$ mm, respectively.

Using the spatial carrier frequency method proposed to consider fringe rotation,[36] the phase difference $\Delta\phi = \phi_{+1} - \phi_{-1}$ is reconstructed from a single captured interferogram. Here, ϕ_{+1} and ϕ_{-1} are the spatial phase distributions of the spherical waves of the ± 1 diffraction orders. The results of the spatial phase shifting is shown in Fig. 5(a) for the s_4 shear measurement. For the wave front reconstruction the phase difference has to be unwrapped. The result of the unwrapping process using PUMA phase unwrapping technique[37] is shown in Fig. 5(b).

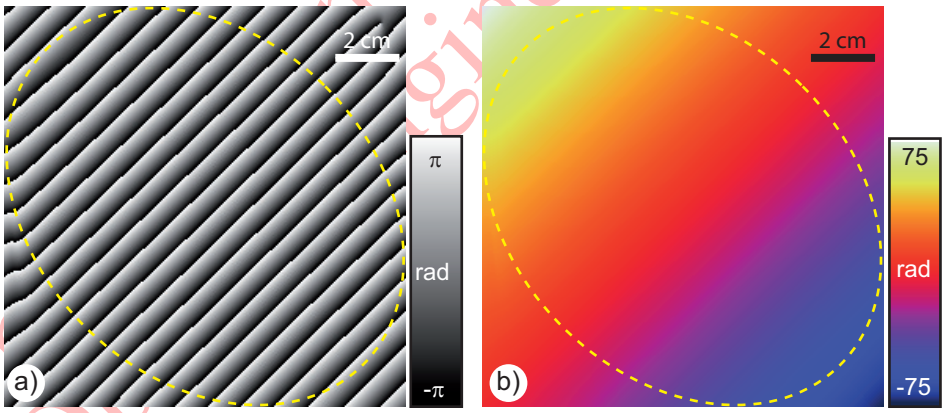

Fig 5 In a) an example of the phase difference reconstructed from the captured interferogram shown in Fig. 4(c) using the spatial carrier frequency approach, while in b) the corresponding phase unwrapped calculated using PUMA phase unwrapping technique. The yellow dashed line oval represents the region of interest where the interference pattern is defined (outside the oval there are areas with low intensity which leads to phase errors, see Fig. 4(c)).

3.2 Wavefront reconstruction

In this section, we describe the method to reconstruct a wavefront from its measured finite differences $\Delta\phi$, which is an ill-posed inverse problem.[38] A solution for the problem was recently

presented and it was achieved by minimizing the following objective function[34,39]

$$L(f) = \sum_{m=1}^{M} \| b(\vec{x}) \left[\Delta_m f(\vec{x}) - \Delta_m \phi(\vec{x}) \right] \| \,, \tag{13}$$

in order to find a wavefront estimate $\tilde{f}$ which minimizes L. In Eq. (13), $\| \cdots \| = \sum_{\vec{x} \in R} | \cdots |^2$ and R refers to the grid of the camera and M represents the number of captured interferograms. Notice, that $b(\vec{x}) = \sqrt{B(\vec{x})}$ is a weighting factor which is defined in Eq. (10) and inherently obtained from the spatial carrier frequency method used to determine $\Delta\phi$ from the captured interference pattern. According to Eq. (13) the sum of the distance squared error (SDS-error) is minimized using $M = 5$ shear measurements where the applied shears in the three shear experiments are $s_1 = [-42, 12.5]$ mm, $s_2 = [-37, 22.5]$ mm, $s_3 = [-30, 32.5]$ mm, $s_4 = [-22.5, 37]$ mm, and $s_5 = [-12.5, 42]$ mm. A gradient-based iterative approach is used in the following to find the minimum of L which represents the least-squares solution of the reconstruction problem.[40] The approach is started with an initial guess $f^{(0)}$. At the l^{th} iteration, the current estimate $f^{(l)}$ maybe written in the form

$$f^{(l)} = f^{(l-1)} - \alpha^{(l-1)} \cdot \nabla L^{(l-1)} \,. \tag{14}$$

We use such an iterative scheme to improve the solution in the direction of the gradient ∇L with a scaling factor $\alpha^{(l-1)}$, which is defined for each iteration.[34] A mathematical formula for the gradient ∇L is explicitly derived in.[39] The iterative scheme stops if the SDS-error exhibits no further improvement, i.e., no changes in the consecutively recovered wavefront. The convergence solution of the minimisation for the first shear experiment is shown in Fig. 6(a), where the stop criteria was reached after 100 iterations.

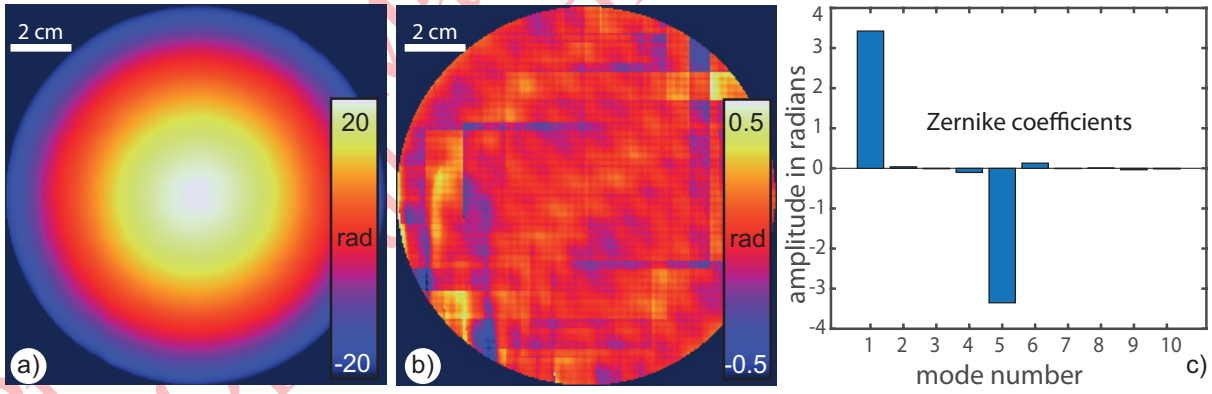

Fig 6 Experimental results: a) and b) wavefront solutions of the iterative scheme for the test spherical wavefront and the residuals after fitting the recovered wavefront using Zernike polynomial decomposition. c) Computed Zernike coefficients of the first 10 Zernike polynomials.

In order to quantitatively evaluate the reconstructed wavefront, a Zernike polynomial decomposition was used.[41,42] This way, wavefront aberrations such as tilt and de-focus, could be accurately evaluated. In addition, the beam radius of curvature of the test spherical wave can be determined. The result of such an evaluation is shown in Fig. 6(b,c) for the first shear experiment. In (b) we show the phase residuals obtained by subtracting the recovered wavefront from the ones recon-

structed from the computed Zernike coefficients which are plotted in (c). From Fig. 6(b) we can estimate a standard deviation of $\sigma = 0.075$ mm which corresponds to approximately $\lambda/14$ root mean square wavefront error. In addition, one can see from Fig. 6(c) that the dominant mode is the 5^{th} one which corresponds to de-focus wavefront aberration, in other words, the wavefront exhibits only spherical aberration as is expected from the first shear experiment. The magnitude of the 5^{th} mode allows us to estimate the beam radius of curvature z which can be calculated from $z = r^2/(4|\mathcal{L}_5|)$,[42] where r is the aperture radius of the measurement. In our experiment, the values $D = 64$ mm and $\mathcal{L}_5 = -3.352$ mm give a beam radius of curvature of 305.49 mm which agrees very well with the geometrical model of the proposed experimental setup presented in Fig. 3.

Figure 7 summarizes the measurements of the distorted wavfronts reconstructed from the second and third shear experiments. In Fig. 7(a) a tilted spherical wavefront is reconstructed while in Fig. 7(b) the applied astigmatism to the spherical wavefront is shown. For a quantitative a assessment of the two wavefronts, Zernike polynomial is again used. The result of this process is shown in Fig. 7(c).

Apart from this aberration, one can see from Fig. 7(c) that the 2^{nd} and 3^{rd} modes which represent the tip tilt of the wave front are the dominant ones and for the case of astigmatism the 4^{th} mode is most significant. These results demonstrate the possibility of measuring wavefront and wavefront aberrations in THz range using a simple experimental setup.

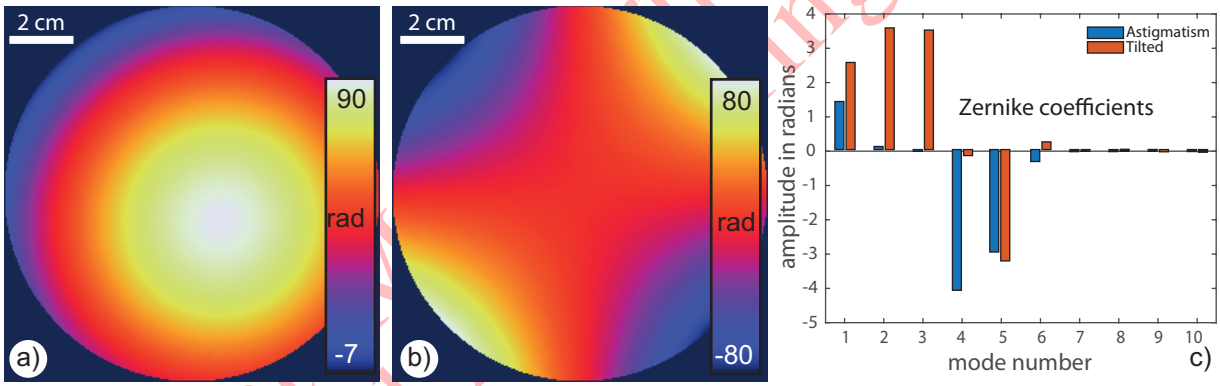

Fig 7 Experimental results of the iteratively reconstructed distorted wavefronts: a) shows a tilted spherical wavefront, while the applied astigmatism to the spherical wavefront is shown in b). In c) the Zernike coefficients for the first 10 Zernike polynomial are given. The graph confirms that the dominant modes are these corresponding to the tip-tilt and astigmatism ones.

4 Conclusions

We have presented a simple THz common-path wavefront sensor based on a phase grating shear interferometer. The setup consists of a phase Ronchi grating located between the THz source and the camera. The phase grating is used to generate a twin image of the test wavefront across the camera plane. We designed and fabricated a grating for optimal operation at 280 GHz. Based on the geometrical parameters of the setup such as the distances between the elements, the wavelength of the THz radiation and the parameters (period and grooves depth) of the Ronci phase grating (RPG) the setup is constructed so that the RPG is used as a shear element generating overlap between ± 1 diffraction orders at the camera plane. Across the overlap zone, the interference pattern is

generated which is captured by the THz camera. The concept is verified by measuring a THz spherical wavefront from 5 shear experiments. These shear experiments where preformed varying the direction of the shear by rotating the RPG. Using the spatial carrier frequency method the phase difference was reconstructed from a single hologram. A gradient-based iterative process was used to recover the test spherical wavefront. We show, that the convergence of the process enables a wavefront reconstruction with a root mean square wavefront error of $\lambda/14$.

Disclosures

The authors declare no conflicts of interest.

Acknowledgments

This work is funded by the Deutsche Forschungsgemeinschaft (DFG) within the project "SensATion" (project no. 423266368). ECC wants to thank the financial support from the Alexander von Humboldt Foundation.

Data, Materials, and Code Availability

Data underlying the presented results may be obtained from the authors upon reasonable request.

References

1 M. Tonouchi, "Cutting-edge terahertz technology," *Nat. Photonics* **1**(2), 97–105 (2007).

2 Y.-S. Lee, *Principles of terahertz science and technology*, vol. 170, Springer Science & Business Media (2009).

3 Z. D. Taylor, R. S. Singh, D. B. Bennett, *et al.*, "THz medical imaging: in vivo hydration sensing," *IEEE Trans. Terahertz Sci. Technol.* **1**(1), 201–219 (2011).

4 A. Soltani, D. Gebauer, L. Duschek, *et al.*, "Crystallization caught in the act with terahertz spectroscopy: Non-classical pathway for l-(+)-tartaric acid," *Chem.-Eur. J.* **23**(57), 14128–14132 (2017).

5 K. Kawase, Y. Ogawa, Y. Watanabe, *et al.*, "Non-destructive terahertz imaging of illicit drugs using spectral fingerprints," *Opt. Express* **11**(20), 2549–2554 (2003).

6 S. Katletz, M. Pfleger, H. Pühringer, *et al.*, "Polarization sensitive terahertz imaging: detection of birefringence and optical axis," *Opt. Express* **20**(21), 23025–23035 (2012).

7 D. M. Mittleman, "Twenty years of terahertz imaging," *Opt. Express* **26**(8), 9417–9431 (2018).

8 C. Jördens and M. Koch, "Detection of foreign bodies in chocolate with pulsed terahertz spectroscopy," *Opt. Eng.* **47**(3), 037003 (2008).

9 L. Valzania, P. Zolliker, and E. Hack, "Topography of hidden objects using THz digital holography with multi-beam interferences," *Opt. Express* **25**(10), 11038–11047 (2017).

10 L. Afsah-Hejri, P. Hajeb, P. Ara, *et al.*, "A comprehensive review on food applications of terahertz spectroscopy and imaging," *Compr. Rev. Food. Sci. Food Saf.* **18**(5), 1563–1621 (2019).

11 M. Agour, C. Fallorf, F. Taleb, *et al.*, "Chocolate inspection by means of phase contrast imaging using multiple plane terahertz phase retrieval," *Opt. Lett.* **47**, 3283–3286 (2022).

12 Q. Sun, Y. He, K. Liu, *et al.*, "Recent advances in terahertz technology for biomedical applications," *Quant. Imaging Med. Surg.* **7**(3), 345 (2017).
13 L. Rong, T. Latychevskaia, C. Chen, *et al.*, "Terahertz in-line digital holography of human hepatocellular carcinoma tissue," *Sci. Rep.* **5**(1), 1–6 (2015).
14 G. G. Hernandez-Cardoso, L. F. Amador-Medina, G. Gutierrez-Torres, *et al.*, "Terahertz imaging demonstrates its diagnostic potential and reveals a relationship between cutaneous dehydration and neuropathy for diabetic foot syndrome patients," *Sci. Rep.* **13**, 3110 (2022).
15 A.-A. A. Boulogeorgos, A. Alexiou, T. Merkle, *et al.*, "Terahertz technologies to deliver optical network quality of experience in wireless systems beyond 5G," *IEEE Commun. Mag.* **56**(6), 144–151 (2018).
16 M. Koch, "Terahertz communications: A 2020 vision," in *Terahertz frequency detection and identification of materials and objects*, R. E. Miles, X.-C. Zhang, H. Eisele, *et al.*, Eds., 325–338, Springer (2007).
17 Y. Ghasempour, R. Shrestha, A. Charous, *et al.*, "Single-shot link discovery for terahertz wireless networks," *Nat. Commun.* **11**(1), 1–6 (2020).
18 K. Sengupta, T. Nagatsuma, and D. M. Mittleman, "Terahertz integrated electronic and hybrid electronic–photonic systems," *Nat. Electron.* **1**(12), 622–635 (2018).
19 M. Abdelghany, A. A. Farid, M. E. Rasekh, *et al.*, "A design framework for all-digital mmwave massive mimo with per-antenna nonlinearities," *IEEE Trans. Wirel. Commun.* **20**(9), 5689–5701 (2021).
20 H.-J. Song and T. Nagatsuma, "Present and future of terahertz communications," *IEEE Trans. Terahertz Sci. Technol.* **1**(1), 256–263 (2011).
21 M. Yamagiwa, T. Minamikawa, F. Minamiji, *et al.*, "Visualization of internal structure and internal stress in visibly opaque objects using full-field phase-shifting terahertz digital holography," *Opt. Express* **27**(23), 33854–33868 (2019).
22 Y. Zhang, C. Wang, B. Huai, *et al.*, "Continuous-wave THz imaging for biomedical samples," *Appl. Sci.-Basel* **11**(1), 71 (2021).
23 N. V. Petrov, J.-B. Perraud, A. Chopard, *et al.*, "Terahertz phase retrieval imaging in reflection," *Opt. Lett.* **45**(15), 4168–4171 (2020).
24 L. Valzania, P. Zolliker, and E. Hack, "Coherent reconstruction of a textile and a hidden object with terahertz radiation," *Optica* **6**(4), 518–523 (2019).
25 L. Rong, S. Wang, D. Wang, *et al.*, "Transport of intensity equation-based terahertz lensless full-field phase imaging," *Opt. Lett.* **46**(23), 5846–5849 (2021).
26 L. Valzania, T. Feurer, P. Zolliker, *et al.*, "Terahertz ptychography," *Opt. Lett.* **43**(3), 543–546 (2018).
27 A. Hamza, A. Belal, T. Sokkar, *et al.*, "Interferometric studies on the influence of temperature on the optical and dispersion parameters of grin optical fibre," *Opt. Lasers Eng.* **45**(1), 145–152 (2007).
28 K. Yassien and M. Agour, "Digital holographic interferometry: optomechanical properties of fibers," *Polym. Eng. Sci.* **51**(6), 1218–1225 (2011).
29 C. Falldorf, M. Agour, C. Von Kopylow, *et al.*, "Phase retrieval for optical inspection of technical components," *J. Opt.* **14**(6), 065701 (2012).

30 C. Falldorf, M. Agour, C. von Kopylow, *et al.*, "Design of an optical system for phase retrieval based on a spatial light modulator," in *AIP Conference Proceedings*, **1236**(1), 259–264, American Institute of Physics (2010).
31 G. Rodríguez-Zurita, N. Toto-Arellano, C. Meneses-Fabian, *et al.*, "Adjustable lateral-shear single-shot phase-shifting interferometry for moving phase distributions," *Meas. Sci. Technol.* **20**(11), 115902 (2009).
32 S. Rasouli and M. Ghorbani, "Nonlinear refractive index measuring using a double-grating interferometer in pump–probe configuration and fourier transform analysis," *J. Opt.* **14**(3), 035203 (2012).
33 M. Agour, C. Falldorf, F. Taleb, *et al.*, "Quasi-optical components for the THz-regime: Fabrication and characterization." DGaO Proceedings **122**, p9, https://www.dgao-proceedings.de/download/122/122_p9.pdf (2021). [Online; accessed 30-June-2022].
34 M. Agour, C. Fallorf, F. Taleb, *et al.*, "Terahertz referenceless wavefront sensing by means of computational shear-interferometry," *Opt. Express* **30**, 7068–7081 (2022).
35 M. Agour, C. Falldorf, F. Taleb, *et al.*, "Shear interferometry for terahertz wavefront sensing," *Proc. SPIE* **12134**, 47–55 (2022).
36 T. Sokkar, K. El-Farahaty, M. El-Bakary, *et al.*, "Characterization of axially tilted fibres utilizing a single-shot interference pattern," *Opt. Lasers Eng.* **91**, 144–150 (2017).
37 J. M. Bioucas-Dias and G. Valadao, "Phase unwrapping via graph cuts," *IEEE Trans. Image process.* **16**(3), 698–709 (2007).
38 M. Servin, M. Cywiak, and A. Davila, "Lateral shearing interferometry: theoretical limits with practical consequences," *Opt. Express* **15**(26), 17805–17818 (2007).
39 C. Falldorf, G. Ehret, M. Schulz, *et al.*, "Wave front characterization of gaussian beams using shear interferometry and a weighted reconstructor," in *DGaO Proceedings 2014*, A11, DGaO (2014).
40 M. Agour, C. Falldorf, and R. B. Bergmann, "Shape measurements of microscopic objects using computational shear interferometry," in *Quantitative Phase Imaging II*, *Proc. SPIE* **9718**, 321–328, SPIE (2016).
41 R. J. Noll, "Zernike polynomials and atmospheric turbulence," *J. Opt. Soc. Am.* **66**(3), 207–211 (1976).
42 T. Binkele, D. Hilbig, T. Henning, *et al.*, "Determination of the paraxial focal length using zernike polynomials over different apertures," in *Photonic Instrumentation Engineering IV*, *Proc. SPIE* **10110**, 60–69, SPIE (2017).

Mostafa Agour is Postdoctoral Research Fellow at the Institute of Applied Beam Technology (BIAS). He was awarded his PhD degree in physics from the University of Bremen in 2011. Currently he is an associate professor at Physics Department, Faculty of Science, Aswan University. He has authored more than 50 journal papers in the field of coherent optical metrology. His recent works particularly include wave-fields sensing using Digital Holography, phase retrieval and shear interferometry, wave fields manipulations and synthesis utilizing spatial light modulators.

Claas Falldorf was awarded his PhD in physics from the University of Bremen in 2009. He has authored more than 50 publications in the field of coherent optics, wave front sensing and signal

processing. He is member of the European technology platform Photonics21 and the Deutsche Gesellschaft für angewandte Optik (DGaO). Currently, he is head of the group Coherent Optics at BIAS. His recent works particularly include sensing of wave fields using phase retrieval and shear interferometry.

Ms. Fatima Taleb received the B.Sc. and MSc degree in communications engineering from the University of Aleppo, Syria in 2010 and 2016, respectively. She worked from 2011 to 2014 as a research assistant at communications engineering department, faculty of electrical and electronic engineering, University of Aleppo, Syria. Since 2018, she has been a research associates at experimental semiconductor physics at the University of Marburg, Germany. Her current research focus on THz communication systems.

Prof. Dr. Enrique Castro-Camus obtained a degree in Physics from Universidad Nacional Autonoma de Mexico in 2002 and a D.Phil (PhD) in Condensed Matter Physics from the University of Oxford in 2006. In 2009 he joined the Centro de Investigaciones en Optica (CIO) in Mexico. In 2021 he was honored with a Guest Professorship at Philipps-Universitat Marburg in Germany. He has taken part as editor and organizer of multiple scientific journals and events. He received the Young Scientist Award from the IRMMW-THz society and the Alexander von Humboldt Experienced Research Fellowship. His research interests include the applications and development of terahertz spectroscopy techniques with particular emphasis on the study of ultrafast charge transport in semiconductors, as well as exploring uses of THz radiation in multiple disciplines such as biology, astronomy, conservation of objects with cultural value, medicine and industry.

Prof. Dr. Martin Koch received the Ph.D. degree in physics from Philipps-Universität Marburg, Marburg, Germany, in 1995, respectively. He was a Post-Doctoral Fellow with Bell Labs/Lucent Technologies, Holmdel, NJ, from 1995 to 1996. From 1996 to 1998, he was with the Photonics and Optoelectronics Group, University of Munich, Munich, Germany. Since 1998, he has been an Associate Professor at the Technische Universität Braunschweig, Braunschweig, Germany. Since 2009, he is full professor of physics with the Philipps-Universität Marburg.

Prof. Dr. Ralf B. Bergmann studied physics in Heidelberg and Freiburg, received his doctorate with his work at the Max Plank Institute for Solid State Research (MPI-FKF) from the University of Stuttgart, worked as a postdoc at of the University of New South Wales and habilitated at the University of Freiburg. After leading a research group at the University of Stuttgart he headed the department of applied physics at the central research and advance engineering facility of the Robert Bosch GmbH and later the physical analyses laboratory in the Automotive Electronics division. Since 2008 he is a professor at the University of Bremen and head of BIAS with the field "Optical Metrology and Optoelectronic Systems".